

See discussions, stats, and author profiles for this publication at: <https://www.researchgate.net/publication/7396634>

# Near Equiatomic FeCo Nanocrystalline Alloy Embedded in an Alumina Aerogel Matrix: Microstructural Features and Related Magnetic Properties

ARTICLE *in* THE JOURNAL OF PHYSICAL CHEMISTRY B · NOVEMBER 2005

Impact Factor: 3.3 · DOI: 10.1021/jp0546554 · Source: PubMed

---

CITATIONS

15

---

READS

12

6 AUTHORS, INCLUDING:



**Giorgio Concas**

Università di Cagliari, Cagliari, Italy

73 PUBLICATIONS 876 CITATIONS

SEE PROFILE



**Francesco Congiu**

Università degli studi di Cagliari

49 PUBLICATIONS 338 CITATIONS

SEE PROFILE



**Anna Corrias**

University of Kent

103 PUBLICATIONS 1,508 CITATIONS

SEE PROFILE

# Near Equiatomic FeCo Nanocrystalline Alloy Embedded in an Alumina Aerogel Matrix: Microstructural Features and Related Magnetic Properties

M. F. Casula,<sup>†</sup> G. Concas,<sup>‡</sup> F. Congiu,<sup>‡</sup> A. Corrias,<sup>†</sup> A. Falqui,<sup>\*,†</sup> and G. Spano<sup>‡</sup>

Dipartimento di Scienze Chimiche and INSTM, Università di Cagliari, S.P. Monserrato-Sestu Km 0.700, I-09042 Monserrato (Cagliari), Italy, and Dipartimento di Fisica, Università di Cagliari and CINSM, S.P. Monserrato-Sestu Km 0.700, I-09042 Monserrato (Cagliari), Italy

Received: August 18, 2005; In Final Form: October 19, 2005

FeCo–Al<sub>2</sub>O<sub>3</sub> nanocomposite aerogels were studied by high-resolution electron microscopy, energy filtered transmission electron microscopy, Mössbauer spectroscopy, and measurements of static magnetizations and hysteretic behavior. The combined use of such techniques provided insights on the formation of bcc FeCo nanocrystalline particles inside the alumina matrix, which is promoted by thermal treatment under hydrogen flow of the parent aerogel. Sample characteristics such as alloy composition and crystallinity, influence of the matrix on the structural evolution, and resulting magnetic properties were investigated as a function of the temperature and time of the reduction treatment.

## Introduction

Iron cobalt alloys in bulk form play an important role in the technology of transformer cores and electrical generators because of their soft ferromagnetic behavior with high Curie temperatures and large saturation inductions, about 15% larger than pure iron.<sup>1,2</sup> In the bulk, Fe and Co form alloys over a wide composition range (at room temperature from pure iron to about 75 at % Co) in the  $\alpha$  body centered cubic (bcc) phase<sup>3</sup> whose structural, magnetic, electric, and mechanical properties have been widely investigated as a function of composition and temperature due to their technological importance.<sup>4</sup>

In particular, the equiatomic alloy exhibits the highest permeability and lowest coercivity and a saturation magnetization close to the highest value, which is observed for the Fe<sub>65</sub>Co<sub>35</sub> composition, and is therefore the most widespread for technological applications.<sup>5</sup>

Because the magnetic properties are strongly influenced by particle size, the stabilization of equiatomic FeCo alloy and in general of iron–cobalt alloys at the nanometer scale has attracted many efforts. The use of additives or the dispersion over a matrix have been proposed to stabilize FeCo alloy. In particular, the preparation of FeCo alloy nanoparticles dispersed in an insulating matrix is attractive for the development of composite-based micro- and nano-devices. Recently, FeCo–SiO<sub>2</sub> and FeCo–Al<sub>2</sub>O<sub>3</sub> nanocomposite materials have been successfully prepared by sol–gel procedures,<sup>6–10</sup> which offer unique advantages in terms of compositional homogeneity, dispersion of the nanophase within the matrix, and of the purity of the resulting material. Aerogel nanocomposites can also be prepared, which in principle allow one to increase the loading of the dispersed phase because of their very extended porosity.

The collective magnetic properties of such nanocomposites are strongly related to their microstructural features such as the size distribution, relative distance, and composition of the alloy

nanoparticles. The microstructure is in turn related to the synthesis conditions and therefore the sample should be carefully characterized at the final and intermediate stages of the preparation.

In this work we present the characterization of the microstructure and the magnetic properties of FeCo–Al<sub>2</sub>O<sub>3</sub> aerogel nanocomposites prepared by a sol–gel procedure followed by a reduction treatment to promote the formation of the alloy.<sup>11</sup> Conventional experimental techniques could not provide a complete picture of the structure of such nanocomposites; in particular the nature of the intermediate phases present in the aerogel prior to the reduction treatment and the amount of FeCo alloy obtained as a function of the temperature and time of the final reduction treatment could not be unambiguously stated.<sup>11</sup> Some more detailed information was derived by separately studying the Fe and Co environment by X-ray absorption spectroscopy, which confirmed unambiguously the formation of bcc FeCo alloy nanoparticles dispersed within the alumina matrix in the final reduced samples; and indicated that Fe(III) and Co (II) ions are present in the aerogel samples prior to reduction and they seem to be located in the vacancies of the defective spinel structure of the  $\gamma$ -Al<sub>2</sub>O<sub>3</sub> matrix.<sup>12</sup>

More detailed microstructural features which may affect the magnetic properties of the nanocomposites, such as the alloy–matrix interface and the composition of the nanoparticles (which may vary when core–shell formation or phase segregation compete with the alloying process), should also be studied in detail. In this paper the magnetic properties of FeCo–Al<sub>2</sub>O<sub>3</sub> nanocomposite aerogels is discussed in relation to their microstructure as obtained by high-resolution electron microscopy (HREM) and ancillary energy filtering (EF) imaging, and by Mössbauer spectroscopy.

## Experimental Details

FeCo–Al<sub>2</sub>O<sub>3</sub> gels were prepared using aluminum tri-*sec*-butoxide (Al(OC<sub>4</sub>H<sub>9</sub><sup>sec</sup>)<sub>3</sub>, Aldrich 97%, ASB) and metal nitrates (Fe(NO<sub>3</sub>)<sub>3</sub>·9H<sub>2</sub>O, Aldrich, 98%, Co(NO<sub>3</sub>)<sub>2</sub>·6H<sub>2</sub>O, Aldrich, 98%) as precursors, and ethanol (Carlo Erba 99.8%, EtOH) as solvent.<sup>11</sup> The total metal amount in the final nanocomposite

\* Corresponding author. Fax: 0039 070 6754388. Tel: 0039 070 6754379. E-mail: falqui@unica.it.

<sup>†</sup> Dipartimento di Scienze Chimiche and INSTM.

<sup>‡</sup> Dipartimento di Fisica.

was 10 wt % ((Fe + Co)/(Fe + Co + Al<sub>2</sub>O<sub>3</sub>)) and the Fe/Co molar ratio was 1:1 for all samples.

The aerogels were obtained by submitting the wet gels to high-temperature supercritical drying in an autoclave (Parr, 300 cm<sup>3</sup>) filled with an appropriate amount of ethanol. The sample obtained after supercritical drying was calcined at 450 °C in static air for 1 h (sample hereafter named C450) and then either further calcined at 900 °C (sample hereafter named C900) or reduced under H<sub>2</sub> flow at temperatures between 700 and 800 °C from 2 to 12 h (samples hereafter named R700\_2h, R700\_12h, and R800\_2h).

High-resolution electron transmission microscopy (HREM) and energy filtered (EF) images were obtained by using a JEOL JEM-2010 high-resolution transmission electron microscope equipped with a LaB<sub>6</sub> cathode and with a Gatan image filter (GIF) spectrometer. The latter allows reconstruction of the image of the sample by collecting only the electrons which have lost energy in a predefined range of the electron energy loss (EELS) spectrum. In an EF image the presence of the selected element appears as a bright zone on a dark background. No sign of beam damage was observed on the samples during investigation.

The Mössbauer absorption spectra were obtained at room temperature in a standard transmission geometry, using a source of <sup>57</sup>Co in rhodium with activity 370 MBq. The calibration was performed using a 6-μm thick natural α-Fe foil; the measured full width at half-maximum of the absorption peak was 0.29 ± 0.01 mm/s. The isomer shift (IS) values are referred to α-Fe. The surface density of the absorbers was 60 mg/cm<sup>2</sup> of sample. The measurements at 293 K were carried out on powder samples contained in a Plexiglas holder. The measurements at 77 K were performed using a liquid nitrogen flow cryostat; the sample holder was kept in exchange gas. All the measurements have been performed with an amount of iron in the samples corresponding to an effective thickness  $t \approx 1$ , smaller than that of the α-Fe foil of calibration, to avoid an excessive peak broadening. The analysis of Mössbauer spectra was performed by fitting the data by peaks of Lorentzian shape and applying a least-squares method.

Measurements of static magnetizations and hysteretic behavior of the samples were performed on a Quantum Design MPMS SQUID magnetometer equipped with a superconducting magnet producing fields up to 50 kOe. Zero-field-cooled (ZFC) magnetizations were measured by cooling samples in zero magnetic field and then by increasing the temperature in an applied field of 25 Oe, while field-cooled (FC) curves were recorded by cooling the samples in the same field of 25 Oe. The field dependence of the magnetization was recorded up to ±50 kOe, at  $T = 4.2$  K.

## Results and Discussion

**HREM and EF Images.** TEM analysis showed that in reduced samples nanoparticles are homogeneously distributed in the alumina matrix, with mean size of around 10 and 15 nm for R700\_12h and R800\_2h, respectively, while for the R700\_2h the size could be simply estimated well below 5 nm.<sup>11</sup>

In Figure 1 the bright field HREM image of one single crystal FeCo alloy nanoparticle in the R800\_2h sample is shown. It can be easily observed as the matrix surrounds and supports the particle, with this peculiar disposition of the particles being the most frequently observed in all the samples. The crystalline planes in the particle have a distance of 0.20 (±0.01) nm, corresponding to the (110) family of the FeCo alloy bcc structure. In the inset of the figure a lower magnification image

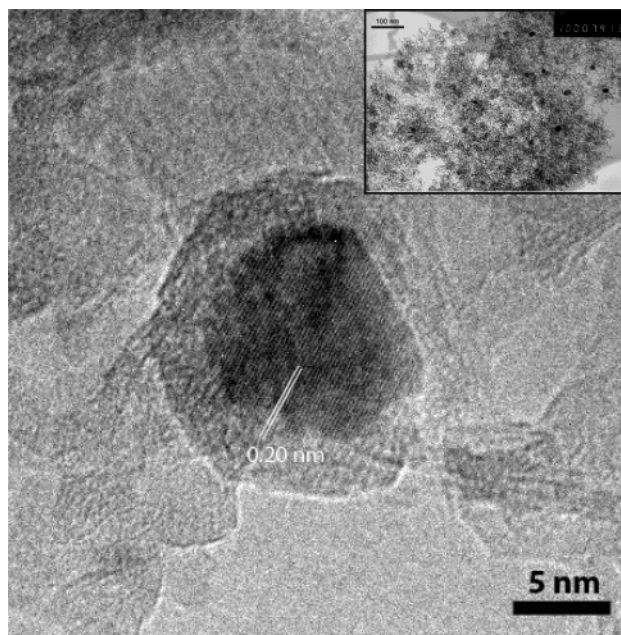


**Figure 1.** High-resolution transmission electron microscopy image of a nanoparticle in the R800\_2h sample. In the inset a lower magnification image is reported.

is reported, where the distance among the nanocrystalline particles can be seen.

The spectral analysis of a representative nanoparticle of the R800\_2h sample was obtained using the GIF spectrometer. Figure 2 shows the bright field HREM image (a), together with the EF images of the same area reconstructed by collecting only the electrons losing energy in the spectral ranges corresponding to the Fe M-edge (b) (94 eV,  $\Delta E = 7$  eV), Co M-edge (c) (101 eV,  $\Delta E = 10$  eV), Al L<sub>2,3</sub>-edge (d) (72 eV,  $\Delta E = 20$  eV), and O K-edge (e) (535 eV,  $\Delta E = 30$  eV). The more pronounced background noise in the latter image is simply due to the reduced intensity of the electrons emitted in correspondence of the O K-edge EELS which lies at higher energies than those of the other elements. These images give a clear picture of the location and distribution of the four elements. Fe and Co are well located inside the nanoparticle: the shape of the central bright zones corresponding to the dark zone in bright field HREM image is similar for the two elements even if the diameter of the bright area is slightly larger for the iron. Iron and cobalt are almost absent elsewhere, with a very limited presence of cobalt around the particle. The aluminum is completely absent inside the particles and present only in the matrix while oxygen is almost completely absent inside the nanoparticle and is mainly located in the alumina matrix.

It should be pointed out that the slightly bigger diameter of the bright zone of the iron EF image with respect to that of the cobalt, together with the shape of the oxygen map, suggests that a thin layer of iron oxide around the particle might be present, even if the higher noise for the oxygen map makes the detection of its presence in such a layer quite difficult. Nevertheless, the oxygen and aluminum show very similar maps, as expected for the Al<sub>2</sub>O<sub>3</sub> matrix.

**Mössbauer Spectroscopy.** To determine the oxidation state of iron in the samples prior to the reduction treatment, the C450 and C900 calcined samples have been investigated by Mössbauer spectroscopy. The spectra of both samples can be fitted by one quadrupole doublet with values of IS (0.32 ± 0.01 and 0.29 ± 0.01 mm/s, respectively) and QS (0.99 ± 0.01 and 0.90 ± 0.01 mm/s, respectively) belonging to trivalent iron.<sup>13,14</sup>



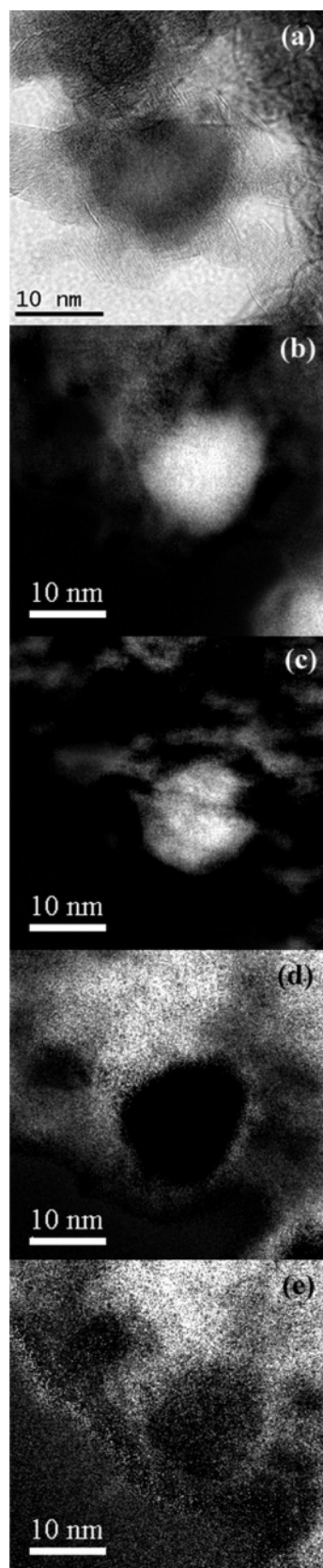


**Figure 2.** Bright field HREM (a) and energy filtered images of the R800\_2h sample corresponding to EELS iron M-edge (b), cobalt-M edge (c), aluminum  $L_{2,3}$ -edge (d), and oxygen K-Edge (e).

The reduced aerogels have been investigated by Mössbauer spectroscopy at 293 and 77 K. In Table 1 the results of the least-squares fits of the spectra at 293 K are given; the values of isomer shift ( $\delta$ ) referred to  $\alpha$ -Fe, quadrupole splitting ( $\Delta$ ),

**TABLE 1: Mössbauer Parameters as Obtained by Fitting the Spectra at 293 K of the Reduced Samples<sup>a</sup>**

sample		$\delta$ mm/s	$\Delta$ mm/s	$\Gamma$ mm/s	B T	area %
R700_2h	I	0.34(1)	1.05(2)	0.74(2)		74(4)
	II	1.00(5)	2.0(1)	0.8(1)		14(4)
	III	0.07(4)		0.6(1)	34.0(9)	12(4)
R700_12h	I	0.33(2)	0.97(5)	0.80(4)		36(2)
	II	0.88(9)	2.08(7)	0.9(1)		13(3)
	III	0.03(1)		0.55(1)	34.8(1)	51(3)
R800_2h	I	0.34(2)	1.00(3)	1.21(4)		32(2)
	II	0.94(3)	2.10(4)	0.49(8)		4(1)
	III	0.02(1)		0.46(1)	34.2(1)	64(3)

<sup>a</sup> The values of isomer shift ( $\delta$ ), quadrupole splitting ( $\Delta$ ), full width at half-maximum of the peaks ( $\Gamma$ ), internal magnetic field ( $B$ ) and relative area of the peaks are given. Statistical errors are given in parentheses as error on the last digit.

**TABLE 2: Mössbauer Parameters at 77 K of the Reduced Samples<sup>a</sup>**

sample		$\delta$ mm/s	$\Delta$ mm/s	B T
R700_2h	I	0.47(1)	1.01(1)	
	II	1.04(2)	2.63(3)	
	III	0.14(3)		35.7(9)
R700_12h	I	0.47(1)	1.06(4)	
	II	1.04(2)	2.63(3)	
	III	0.13(1)		35.7(1)
R800_2h	IV	0.48(4)		47.5(3)
	I	0.56(2)	1.10(6)	
	II	1.04(2)	2.63(3)	
	III	0.12(1)		35.0(1)
	IV	0.48(4)		47.5(3)

<sup>a</sup> The values of isomer shift ( $\delta$ ), quadrupole splitting ( $\Delta$ ), and internal magnetic field ( $B$ ) are given. Statistical errors are given in parentheses as errors on the last digit.

full width at half-maximum ( $\Gamma$ ), hyperfine internal magnetic field ( $B$ ) and relative area of the components are reported. Table 2 reports the parameters at 77 K resulting from the fits of the spectra at low temperature.

In Figure 3a the spectrum of the R800\_2h sample at 293 K is shown. The spectrum shows three components; the experimental data can be fitted by one sextet and two quadrupole doublets with different isomer shift (IS). The components correspond to iron in three different oxidation states: the value of IS of the sextet (component III) is typical of iron with oxidation number equal to zero, while the value of IS and quadrupole splitting (QS) of the doublets belong to trivalent iron (component I) and bivalent iron (component II),<sup>13,14</sup> about 64% of Fe atoms are in metallic form. The sextet (component III) has values of IS and hyperfine field (HF) which are typical of FeCo alloys.<sup>15</sup> In these materials, the HF changes with the composition of the alloy with a maximum value at 70–75 at. % of Fe. The field  $B = 34.2 \pm 0.1$  T corresponds to the alloy composition  $\text{Fe}_{48}\text{Co}_{52}$ ; the other possible composition (less than 10 at. % of Co) was rejected because it is very different from the nominal one. This value of the HF, which is very different with respect to the pure bcc iron ( $B = 33.3$  T),<sup>16</sup> gives the experimental evidence of the formation of the alloy. The full width at half-maximum (fwhm) of the absorption peaks of the sextet should be compared with the value of the bulk crystalline alloy, which has a width similar to pure metallic iron (0.29 mm/s for  $\alpha$ -Fe in our experimental conditions).<sup>15</sup> The value of  $0.46 \pm 0.01$  mm/s observed in this case can be attributed to the superparamagnetic broadening of the peaks,<sup>17,18</sup> because it increases in the sequence R800\_2h, R700\_12h, and R700\_2h

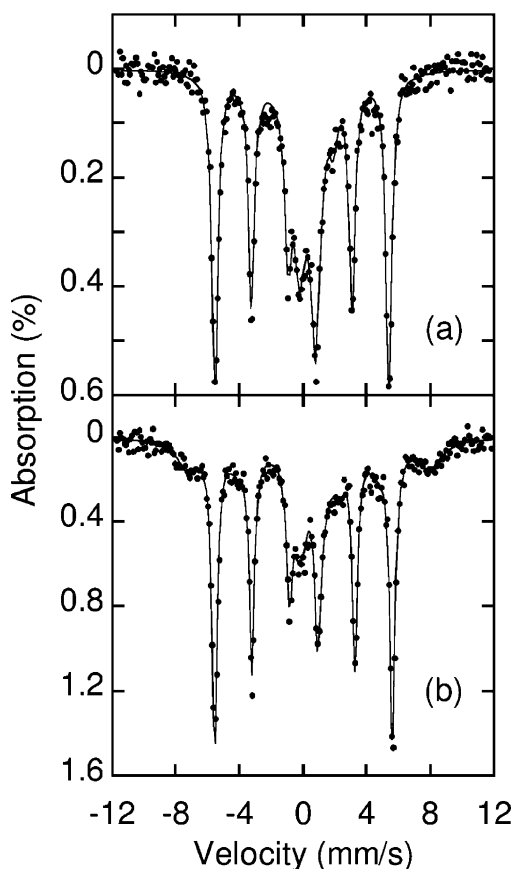


**Figure 3.** Mössbauer spectra of the R800\_2h sample at 293 K (a) and at 77 K (b). The experimental points are reported as dots; the fitting curve is shown as a continuous line.

as the size of the alloy nanoparticles decreases, previously evidenced by X-ray diffraction and conventional TEM.<sup>11</sup>

The component I has values of IS and QS which are common to different iron oxides and oxyhydroxides in nanocrystalline form,<sup>18–21</sup> while the component II has values of IS and QS typical of a bivalent iron phase.<sup>14</sup>

Figure 3b shows the spectrum of the sample R800\_2h at 77 K. It shows the same features of the spectrum at room temperature with the appearance of a magnetically ordered phase with trivalent iron. This phase (component IV) has shift  $\delta = 0.48 \pm 0.04$  mm/s and field  $B = 47.5 \pm 0.3$  T; these values could be ascribed to a spinel structure similar to that of the matrix,  $\gamma$ -Al<sub>2</sub>O<sub>3</sub>, where Fe(III) substitutes Al(III),<sup>18</sup> whose presence was supposed as a result of EXAFS characterization.<sup>12</sup> This phase is superparamagnetic at room temperature and magnetically blocked at 77 K in this sample.

Figure 4a shows the spectrum of the R700\_12h sample at 293 K. The spectrum of this sample shows the same features of the spectrum of the R800\_2h sample. The HF of component III has a value of  $34.8 \pm 0.1$  T, which corresponds to the alloy composition Fe<sub>56</sub>Co<sub>44</sub>,<sup>15</sup> about 51% of the Fe atoms have oxidation number equal to zero. Therefore there is a smaller amount of alloy with respect to the sample R800\_2h; indicating that the reduction at 800 °C for 2 h is more effective than the reduction at 700 °C for 12 h. In the spectrum of the R700\_12h sample at 77 K appears the magnetically ordered phase (component IV) of trivalent iron found in the R800\_2h sample, as shown in Figure 4b.

In Figure 5 the spectra of the R700\_2h sample at 293 K (Figure 5a) and at 77 K (Figure 5b) are shown. The components appearing in the spectra are the same as those found in the other

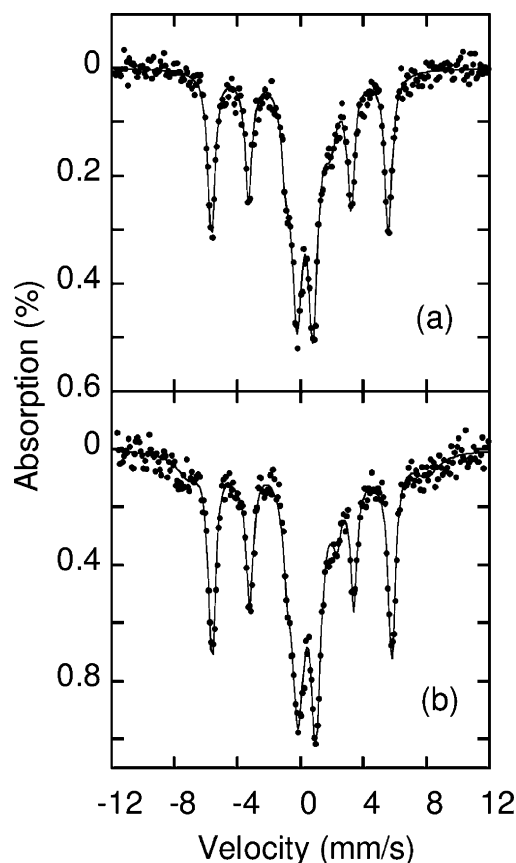


**Figure 4.** Mössbauer spectra of the R700\_12h sample at 293 K (a) and at 77 K (b). The experimental points are reported as dots; the fitting curve is shown as a continuous line.

reduced samples; at 77 K there is no trace of the magnetically ordered trivalent iron phase. The HF value of the alloy (component III) has a rather large experimental uncertainty at 293 and 77 K, but its value is in the range of the other two samples; therefore we expect that the alloy composition is in the same range. About 12% of the Fe atoms have oxidation number equal to zero; the amount of alloy is the smallest in the reduced samples.

The determination of the composition has been performed according to the HF dependence on the composition as reported for FeCo bulk alloys.<sup>15</sup> To verify if the HF value is influenced by the nanometer size of the FeCo particles, Mössbauer measurements were performed also on an Fe–Al<sub>2</sub>O<sub>3</sub> nanocrystalline sample with 10 wt % of iron, which was prepared using the same procedure as the FeCo–Al<sub>2</sub>O<sub>3</sub> samples under study. The spectrum of this sample at room temperature shows an ordered component whose magnetic field has a value of 33.3 T, which equals the value for bulk  $\alpha$ -iron. Therefore the values of HF measured in this work for the nanocrystalline FeCo alloy can be easily differentiated with respect to the HF of the nanocrystalline  $\alpha$ -Fe.<sup>22</sup>

Therefore the Mössbauer characterization indicates that the reduction of trivalent iron in hydrogen flow begins at 700 °C but it is not complete even after a treatment at 800 °C for 2 h, since only  $2/3$  of the iron is present as metallic iron; a fraction of the residual is reduced to divalent iron. The duration of the reduction treatment (2 or 12 h) and the reduction temperature (700 or 800 °C) modify the amount of the reduced iron and the composition of the nanocrystalline FeCo alloy; the best result is obtained by increasing the reduction temperature. These results are consistent with those obtained by Fe and Co K-edge EXAFS,<sup>12</sup> which estimated a larger fraction (85%) of reduced

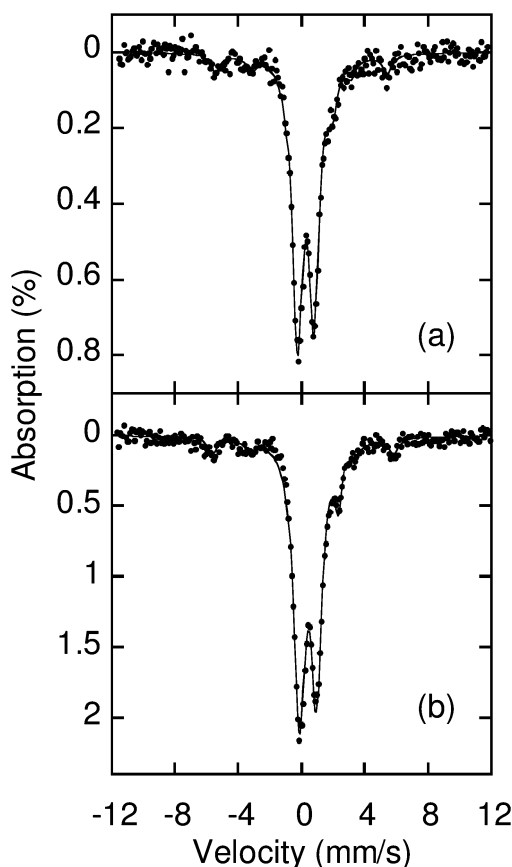


**Figure 5.** Mössbauer spectra of the R700\_2h sample at 293 K (a) and at 77 K (b). The experimental points are reported as dots; the fitting curve is shown as a continuous line.

iron in the sample reduced for 2 h at 800 °C, if the experimental uncertainties of the two techniques are taken into account.

**Magnetic Characterization.** The magnetic characterization of the samples was first investigated by measuring the ZFC and FC magnetization curves.

In the case of superparamagnetic behavior, at high temperature the ZFC and FC magnetization curves overlap and follow, as a first approximation, a Curie–Weiss law<sup>23–25</sup>

$$M = \frac{M_s^2(T)H}{3k_B \langle V \rangle (T - \theta)} \quad (1)$$

where  $M_s$  is the saturation magnetization,  $k_B$  is the Boltzmann's constant,  $\langle V \rangle$  is the mean nanoparticle volume,  $T$  is the absolute temperature, and  $\theta$  is the superparamagnetic Curie temperature. At low temperature the curves begin to separate and the ZFC magnetization curve exhibits a broad maximum.

It is generally assumed that the temperature of the ZFC maximum,  $T_{\max}$ , is directly proportional to the average blocking temperature,  $T_{\max} = \beta T_B$ , where  $\beta$  is a constant depending on the shape of the size distribution; therefore,  $T_{\max}$  corresponds to the blocking of particles with the mean size.<sup>26,27</sup>  $T_{\max}$ , however, might not be detectable in the investigated range. The temperature at which the ZFC and FC curves begin to separate ( $T_{\text{sep}}$ ) corresponds to the blocking of the largest particles. The difference ( $T_{\text{sep}} - T_{\max}$ ) is therefore a qualitative measure of the width of the energy barrier distribution and thus of the nanoparticle size distribution.

The ZFC and FC magnetizations of the C450 and C900 aerogels (not reported here) are very similar and they show a

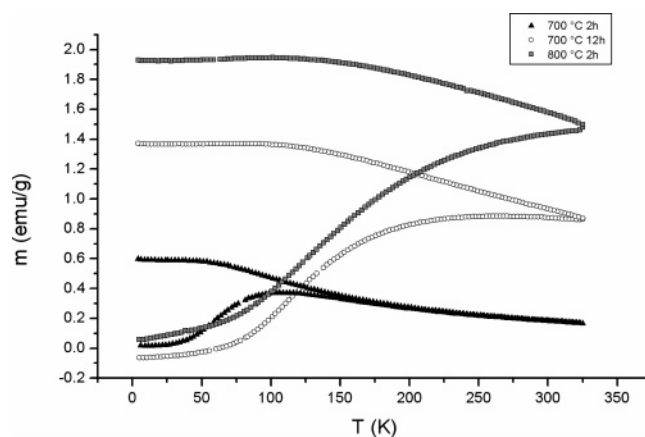


**Figure 6.** ZFC and FC static magnetizations for the R700\_2h (▲), R700\_12h (○), and R800\_2h (■) samples obtained with a magnetic field of 25 Oe.

pure paramagnetic behavior. Only in the case of the reduced aerogels does the superparamagnetic behavior appear as a consequence of the formation and growth of the metal ferro-magnetic nanoparticles within the matrix.

Figure 6 reports the ZFC and FC static magnetization of the R700\_2h, R700\_12h, and R800\_2h samples, measured in the temperature range of 4.2–325 K in an applied field of 25 Oe. Since the amount of the FeCo alloy in the samples can vary with time and temperature of the reduction treatment, the magnetic data were normalized with respect to the total sample mass of the sample.

The three pairs of ZFC–FC curves present significant shapes. In particular, the R700\_2h sample shows the typical superparamagnetic behavior: a well-defined maximum, at  $T_{\max} \approx 100$  K, can be identified in the ZFC curve and above  $T_{\text{sep}} \approx 160$  K the ZFC and FC magnetizations are completely superimposed. This implies that for temperatures higher than 160 K all the nanoparticles are—with respect to the proper measurement's time of static magnetization—in superparamagnetic state, i.e. their magnetic moments can freely oscillate between two opposite directions of easy magnetization.

On the other hand, the ZFC–FC curves of the R700\_12h and R800\_2h samples are not yet superimposing at  $T = 325$  K, indicating the presence of nanoparticles that at this temperature are still in the magnetic blocked state. Together with the modification of their shape, the three pairs of ZFC–FC curves show an increment in the values of magnetization with increasing time and temperature of the thermal treatment, which can be mainly ascribed to the formation and growth of the FeCo nanoparticles. Such a trend can be related to the increase of the mean value and width of the particle diameter distribution, which was evidenced by TEM and XRD measurements,<sup>11</sup> and also to the increase of magnetic interparticle interactions strength. A rough estimate of the interparticle interaction strength could be obtained by analyzing the magnetizations in the thermal range where the ZFC and FC curves are completely superimposed only in the case of the R700\_2h. Because for temperature higher than 160 K a deviation from the Curie–Weiss law is present, due to the thermal dependence of the magnetic moment, a thermal correction for  $M_s$  had to be introduced. In particular, the temperature dependence of  $M_s$  can be reproduced by Bloch's law:

$$M_s(T) = M_s(T = 0 \text{ K})(1 - DT^{3/2}) \quad (2)$$

where  $M_s(T = 0 \text{ K})$  is the zero temperature magnetization and



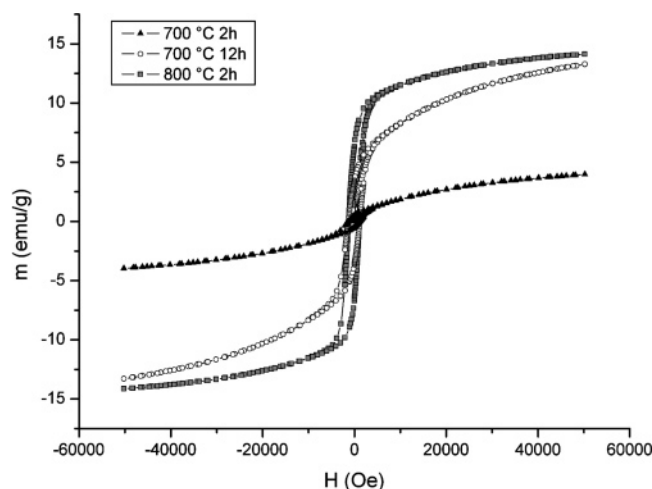


**Figure 7.** Field dependence of the magnetizations recorded at 4.2 K for the R700\_2h (▲), R700\_12h (○), and R800\_2h (■) samples.

**TABLE 3: Parameters Obtained by the Magnetic Characterization of the Samples, Either from Experiment or from Fitting the ZFC–FC and the Hysteresis Curves<sup>a</sup>**

sample	$M_S$ (emu·g <sup>-1</sup> )	$M_r$ (emu·g <sup>-1</sup> )	$M_r/M_S$	$H_c$ (Oe)	$T_{max}$ (K)	$T_{sep}$ (K)	$\theta$ (K)
700 °C 2 h	5(1)	0.49(2)	0.1	1266(8)	100(5)	260(5)	101(7)
700 °C 12 h	17(2)	3.44(2)	0.2	1239(8)	n.d.	n.d.	n.d.
800 °C 2 h	15.7(5)	6.30(2)	0.4	1174(8)	n.d.	n.d.	n.d.

<sup>a</sup> Saturation magnetization ( $M_S$ ), remanent magnetization ( $M_r$ ), reduced remanent magnetization ( $M_r/M_S$ ), coercive field ( $H_c$ ), temperature corresponding to the ZFC curve maximum ( $T_{max}$ ) and to the separation between ZFC and FC curves ( $T_{sep}$ ), Curie's superparamagnetic temperature ( $\theta$ ). n.d.: not determined. Errors are given in parentheses as errors on the last digit.

$D$  is the so-called spin wave constant, that take into account the misalignment of the magnetic moments due to the thermal energy.<sup>27</sup>

By fitting the FC curve of the R700\_2h sample between 295 and 325 K a  $\theta$  value of 101 K was obtained, confirming the presence of interparticle interactions. Although by analogy to paramagnetism it is normally assumed that  $\theta$  is related to interparticle interactions, Dormann et al. verified that it also depends on the sample shape, the geometry of the experiment and the applied field, the  $\theta$  value giving therefore only a qualitative indication of the presence of interparticle interactions in this sample.<sup>28,29</sup> The observation that the FC curve of all the samples at low temperature is almost constant gives further evidence of the occurrence of interparticle interactions. This behavior can be ascribed to a transition to a magnetic collective state.<sup>30</sup>

To further magnetically characterize the samples, magnetization vs field curves (hysteresis loops) were obtained at the fixed temperature of 4.2 K, i.e., well below the  $T_{max}$  of all three samples. In Figure 7 the hysteresis loops are shown, and in Table 3 all the corresponding characteristic parameters are reported. The shape of the hysteresis loops changes as a function of time and temperature of the reduction treatment. In particular, it is evident that for the R700\_2h sample, the hysteresis is farther off from the saturation than in the other samples. This clearly indicates that the mean nanoparticle diameter increases by increasing time and temperature of thermal treatment: as the low-field part of the hysteresis loop is controlled by the magnetic blocking of the largest particles, the sample with the largest amount of large nanoparticles will reach the saturation readily (i.e., at lower field values). The hysteresis curves of all the

samples do not reach complete saturation even at 50 kOe. The observed hysteretic behavior is in agreement with the results obtained by TEM analysis,<sup>11</sup> where particles were barely observed in the sample R700\_2h, while they were clearly revealed in the other two, with the nanoparticle mean diameter being the largest in the R800\_2h sample.

To obtain an estimation of the saturation magnetization values ( $M_S$ ), the high field  $M$  values vs  $1/H$  were plotted, as reported in ref 31. The  $M_S$  values, reported in Table 3, were obtained by extrapolating the curves fitted with a spline function and taking the value corresponding to  $1/H = 0$ . It should be pointed out that the uncertainty of the  $M_S$  values is larger for the samples farther from saturation.

The reduced remanence magnetization ( $M_r/M_S$ ) values reported in Table 3 are lower than 0.5, the value expected for randomly oriented, blocked nanoparticles. This discrepancy can be mainly ascribed to the occurrence of a nonnegligible fraction of small particles which are still relaxing fast at 4.2 K or to a fraction of free paramagnetic Fe and Co ions. Moreover, the ( $M_r/M_S$ ) values for the R700\_12h and R800\_2h samples are significantly different, the latter being the largest. This is in agreement with X-ray diffraction and conventional TEM measurements that pointed out that the size of the nanoparticles increases with time and temperature of the thermal treatment.<sup>11</sup> The FC hysteresis loops can give evidence of the presence of antiferromagnetic (AFM)–ferromagnetic (FM) exchange interaction in the samples, such a case being quite likely with the presence of an AFM external oxide layer on the FM core of the nanoparticles.<sup>32–34</sup> In fact, if AFM–FM interactions are present, by field cooling the system through its blocking temperature, a shift of the hysteresis loops appears. To this end, the reduced samples were cooled under an external magnetic field of +50 kOe, before measuring again the hysteresis loops. The result of these measurements is reported in Figure 8 a, b, and c, where it can be observed that the effect on the FC curve is to modify the positive remanent magnetization ( $M_r$ ) and the negative coercive field ( $H_c$ ), while no modification is observed in the increasing part of the hysteresis loops, which is obtained after reaching the highest negative field (–50 kOe). Therefore, the occurrence of AFM–FM exchange interaction can be ruled out since the observed behavior is the consequence of preferential orientation of the nanoparticles ensemble along the positive direction of the field applied during the FC, which modifies both positive  $M_r$  and negative  $H_c$ . When the highest negative field is reached such preferential orientation is destroyed, and therefore the final increasing part (from –50 to +50 kOe) of the hysteresis loops does not show any difference with respect to the one measured after the ZFC procedure.

If the only magnetic phase in the samples is the FeCo alloy, by comparison of the  $M_S$  values extrapolated at 4.2 K, which are reported in Table 3, with that of the bulk FeCo alloy, the percentage of alloy in the R800\_2h, R700\_12h, and R700\_2h samples can be estimated to be  $68 \pm 2$ ,  $73 \pm 8$ , and  $21 \pm 4$ , with respect to the expected alloy amount. It should be noted that only the percentage obtained for the R800\_2h sample is in agreement with the findings of Mössbauer spectroscopy. However, it should be pointed out that Mössbauer spectroscopy gives directly the amount of iron present as metallic iron, while the  $M_S$  values can be influenced by the presence of additional magnetic phases. Even if the presence of AFM phases can be ruled out on the basis of the FC hysteresis loops, a contribution to the total magnetization can stem from the magnetic phases containing trivalent iron, which were evidenced by Mössbauer spectroscopy, or cobalt, which cannot be evidenced by Möss-

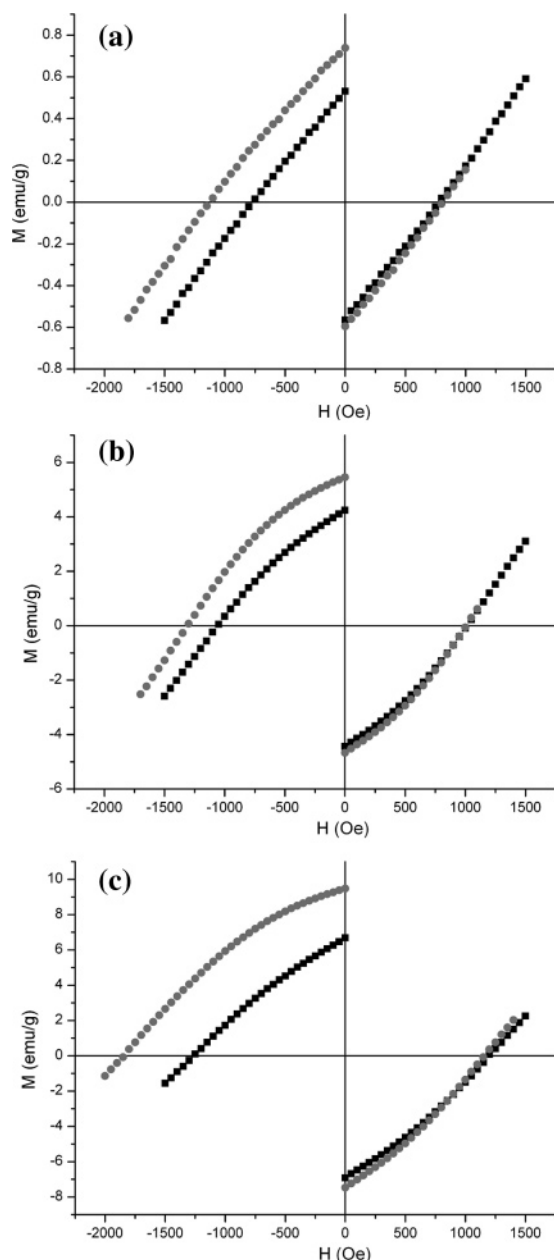


**Figure 8.** ZFC (■) and FC (●) hysteresis loops of the R700\_2h (a), R700\_12h (b), and R800\_2h (c) samples. The FC hysteresis were measured after field cooling in an applied field of 50 kOe.

bauer spectroscopy. Moreover, the fact that the Mössbauer spectra and the hysteresis loops were collected at very different temperatures can have a great influence on the samples in which the fraction of particles that are superparamagnetically relaxing is growing with temperature, as it is the case for the R700\_12h and R700\_2h samples.

Having found evidence of the occurrence of interparticle interactions in the samples, it is also necessary to understand if they are dipolar interactions, or direct exchange interaction. On the basis of all the results here reported, the interparticle interactions in the samples should be mainly dipolar-like, with the direct exchange interaction being quite unlikely due to the low probability of direct contact among the particles, as confirmed by TEM observations.<sup>11</sup> In particular, the FeCo alloy nanoparticles are small and their mean distance is large enough to avoid contact due to the large porosity of the matrix. We can gather some more insight from the variation of the reduced remanent magnetization ( $M_r/M_s$ ) and of the coercive field  $H_c$

with the time and temperature of final reduction treatment. These values are, in fact, influenced in a different way by the alloy amount and by the mean nanoparticle diameter. In particular, the dipolar interparticle interaction strength increases with the alloy amount since the mean distance among the particles decreases giving rise to a decrease in ( $M_r/M_s$ ) and  $H_c$  values.<sup>35</sup> On the other hand, if dipolar interparticle interaction strength increases due to a larger mean particle diameter (and therefore mean particle magnetic moment) a decrease in  $H_c$  value accompanied by an increase in  $M_r/M_s$  value is expected. In the present case a slight decrease in the values of  $H_c$  and an increase in the values of ( $M_r/M_s$ ) is observed going from the R700\_2h to the R800\_2h sample, suggesting that the predominant effect is the increase of the nanoparticle mean size.

## Conclusions

The characterization of FeCo–Al<sub>2</sub>O<sub>3</sub> nanocomposite aerogels by HREM and EF imaging indicates that single-crystal FeCo alloy nanoparticles are formed inside the matrix.

Mössbauer spectroscopy indicates that reduction of iron in the aerogels begins after a thermal treatment in hydrogen flow at 700 °C. The reduction gives rise to the formation of metallic iron and also divalent iron. The amount of reduced iron increases when the treatment is protracted for a longer time and further increases with the treatment at 800 °C. However, the reduction is not complete even at the latter temperature. The composition of the FeCo alloy nanoparticles slightly changes around the equimolar composition, as a function of the temperature and time of the reduction treatment, as a result of the different response of iron and cobalt ions to the reduction treatment.

The magnetic characterization of the reduced samples indicates that the mean blocking temperature depends on the average size of the FeCo alloy nanoparticles which increases with time and temperature of the reduction treatment. In particular, the samples treated at 700 °C for 12 h and at 800 °C for 2 h are in the magnetic blocked state still at room temperature. The presence of dipolar interparticle interactions was evidenced.

**Acknowledgment.** We acknowledge Ministero dell'Istruzione, Università e Ricerca (MIUR PRIN) for financial support.

## References and Notes

- (1) MacLaren, J. M.; Schulthness, T. C.; Butler, B. H.; Sutton, R.; McHenry, M. J. *J. Appl. Phys.* **1999**, *85*, 4833.
- (2) Saad, A. M.; Mazanik, A. V.; Kalinin, Yu. E.; Fedotova, J. A.; Fedotov, A. K.; Wrotek, S.; Sitnikov, A. V.; Svito, I. A. *Rev. Adv. Mater. Sci.* **2004**, *8*, 152A.
- (3) Fernandez-Guillermot, A. *High Temp. High Press.* **1988**, *19*, 477.
- (4) Bardos, D. I. *J. Appl. Phys.* **1969**, *40*, 1371.
- (5) Paduani, C.; Krause, J. C. *J. Appl. Phys.* **1989**, *86*, 578.
- (6) Brinker, C. J.; Scherer, G. W. *Sol–Gel Science*; Academic Press: San Diego, CA, 1990.
- (7) Ennas, G.; Casula, M. F.; Falqui, A.; Gatteschi, D.; Marongiu, G.; Piccaluga, G.; Sangregorio, C.; Pinna, G. *J. Non-Cryst. Solids* **2001**, *293*, 1.
- (8) Casula, M. F.; Corrias, A.; Paschina, G. *J. Mater. Chem.* **2002**, *12*, 1505.
- (9) Casula, M. F.; Corrias, A.; Falqui, A.; Serin, V.; Gatteschi, D.; Sangregorio, C.; De Julián Fernández, C.; Battaglin, G. *Chem. Mater.* **2003**, *15*, 2201.
- (10) Ennas, G.; Falqui, A.; Marras, S.; Sangregorio, C.; Marongiu, G. *Chem. Mater.* **2004**, *16*, 5659.
- (11) Corrias, A.; Casula, M. F.; Falqui, A.; Paschina, G. *Chem. Mater.* **2004**, *16*, 3130.
- (12) Corrias, A.; Navarra, G.; Casula, M. F.; Marras, S.; Mountjoy, G. *J. Phys. Chem. B* **2005**, *109*, 13964.
- (13) Gutlich, P.; Link, R.; Trautwein, A. *Mössbauer Spectroscopy and Transition Metal Chemistry*; Springer-Verlag: Berlin, 1978; p 56.
- (14) Darby Dyar, M. *Am. Mineral.* **1985**, *70*, 304.



- (15) Johnson, C. E.; Ridout, M. S.; Cranshaw, T. E. *Proc. Phys. Soc.* **1963**, *81*, 1079.
- (16) Danon, J. In *Chemical Applications of Mössbauer Spectroscopy*; Goldanskii, V. I., Herber, R. H., Eds.; Academic Press: New York, 1968; p 159.
- (17) Wickman, H. H. In *Mössbauer Effect Methodology*; Gruverman, I. J., Ed.; Plenum Press: New York, 1966; Vol 2, p 39.
- (18) Cannas, C.; Concas, G.; Gatteschi, D.; Falqui, A.; Musinu, A.; Piccaluga, G.; Sangregorio, C.; Spano, G. *Phys. Chem. Chem. Phys.* **2001**, *3*, 832.
- (19) Murad E.; Johnston, J. H. In *Mössbauer Spectroscopy Applied to Inorganic Chemistry*; Long, G. J., Ed.; Plenum: New York, 1987; Vol 2, p 507.
- (20) Suzdalev, I. P.; Buratsev, V. N.; Imshennik, V. K.; Maksimov, Y. V.; Matveev, V. V.; Novichikhin, S. V.; Trautwein, A. X.; Winkler, H. Z. *Z. Phys. D* **1996**, *37*, 55.
- (21) Concas, G.; Ennas, G.; Gatteschi, D.; Musinu, A.; Piccaluga, G.; Sangregorio, C.; Spano, G.; Stanger, J. L.; Zedda, D. *Chem. Mater.* **1998**, *10*, 495.
- (22) Concas, G.; Congiu, F.; Ennas, G.; Piccaluga, G.; Spano, G. *J. Non-Cryst. Solids* **2003**, *330*, 234.
- (23) Morrish, A. H. *The Physical Principles of Magnetism*; Wiley: New York, 1965.
- (24) Nèel, L. *Ann. Geophys.* **1949**, *5*, 99.
- (25) Chantrell, R. W.; Wohlfhart, E. P. J. *J. Magn. Magn. Mater.* **1983**, *40*, 1.
- (26) Gittleman, J. I.; Abeles, B.; Bozowski, S. *Phys. Rev. B* **1974**, *9*, 3891.
- (27) El-Hilo, M.; O'Grady, K.; Chantrell, R. W. *J. Magn. Magn. Mater.* **1992**, *117*, 21.
- (28) Dormann, J. L.; Fiorani, D. *J. Magn. Magn. Mater.* **1995**, *140*, 415.
- (29) Dormann, J. L. In *Magnetic Properties of Fine Particles*; North-Holland: Amsterdam, 1992; p 115.
- (30) Fiorani, D.; Dormann, J. L.; Cherkaoui, R.; Tronc, E.; Lucari, F.; D'Orazio, F.; Spinu, L.; Nogues, M.; Garcia, A.; Testa, A. M. *J. Magn. Magn. Mater.* **1999**, *196–197*, 143.
- (31) Ahmed, S. R.; Ogale, S. B.; Papaefthymiou, G. C.; Ramesh, R.; Kofinas, P. *Appl. Phys. Lett.* **2002**, *80*, 1616.
- (32) Hanson, M.; Johansson, C.; Pedersen, M. S.; Mørup, S. *J. Phys.: Condens. Mater.* **1995**, *7*, 9269.
- (33) Chudnovsky, E. M. *J. Appl. Phys.* **1988**, *64*, 5770.
- (34) Nogués J.; Schuller, I. K. *J. Magn. Magn. Mater.* **1999**, *192*, 203.
- (35) Chantrell, R. W.; Coverdale, G. N.; El-Hilo, M.; O'Grady, K. *J. Magn. Magn. Mater.* **1996**, *157–158*, 250.